Thermodynamic modeling of complex solid solutions in the Lu-H-N system via graph neural network accelerated Monte Carlo simulations

Pin-Wen Guan,* Catalin D. Spataru, Vitalie Stavila, Reese Jones, Peter A. Sharma, and Matthew D. Witman†
Sandia National Laboratories, Livermore, California 94551-0969, United States
(Dated: August 18, 2024)

Metal hydrides are important across diverse applications such as hydrogen storage, batteries, gas sensors, nuclear reactions and high-temperature superconductivity. Previous computational studies of metal hydrides under extreme pressures, e.g., $O(10^2)$ GPa, usually treat them as stoichiometric compounds without considering interstitial lattice disorder. As pressures become more moderate in the $O(10^0)$ GPa and below range, hydrogen disorder at interstitial lattice sites becomes prominent, e.g. in the N-doped Lu hydride that was recently claimed superconducting near 1 GPa. Further adding compositional complexity from alloying and/or multi-element interstitial occupation makes elucidating pressure- and temperature-dependent observables intractable by first-principles calculations alone. We therefore propose a lattice graph neural network surrogate modeling approach to predict configuration- and pressure-dependent equation-of-state properties. Their efficiency permits Monte Carlo simulations to calculate Gibbs energies and pressure-dependent phase diagrams, thereby revealing insights into the synthesis conditions required for achieving desired phase equilibria. We demonstrate this concept for the compositionally complex cubic $Lu(H, N, Va)_3$ system where three constituents (hydrogen, nitrogen and vacancy) have disordered multi-element interstitial occupancies and insights into pressure-dependent phase equilibria are critically needed, e.g., N-doping levels can significantly lower dehydrogenation temperatures and provide a new strategy to optimize hydrogen-storage alloys. This work can improve the thermodynamic understanding of the Lu-H-N system and help rational synthesis of N-doped Lu hydrides, but more generally demonstrates an efficient approach to model pressure-dependent thermodynamics of multi-component solid solutions.

INTRODUCTION

Enormous progress has been made in recent years in the pursuit of room-temperature superconductors, mainly driven by metal hydrides. Near-room-temperature superconductor was predicted [1, 2], synthesized [3], discovered [4] and subsequently confirmed [5] in the La-H system for the first time. In addition, the same theoretical techniques that led to the discovery of superconductivity in LaH_{10} predict even higher-temperature superconductors such as Li_2MgH_{16} with T_c as high as ∼470 K at 250 GPa [6]. However, creation of these superhydrides requires megabar (> 100 GPa) pressure, which is a significant hurdle for large-scale synthesis. Therefore, lowering the pressure for synthesizing these novel materials is a crucial milestone in the pursuit of practical room-temperature superconductivity [7], with several approaches proposed, including optimized chemical precompression [8], impurity doping in hydrides [9–12], and combining multiple stimuli (e.g., pressure and electrochemical potential) [13, 14]. An especially remarkable report was the claim of room-temperature superconductivity at near-ambient pressures in N-doped Lu hydrides [15], which subsequently stimulated a rush [16–25] trying to clarify and reproduce the superconducting phase whose structure is reported to have a fcc Lu lattice but with undetermined stoichiometry and atomic positions of H and N. However, these verification efforts, no matter experimental or computational, have not reproduced the claim and the original study has since been retracted.

Nonetheless, the open question of how N, along with H, is incorporated into the interstitials of the Lu FCC lattice remains. Specifically, the pressure-composition-temperature (PCT) phase behavior of the Lu-N-H system has yet to be predicted, i.e., the expected N and H concentrations as a function of N and H chemical potentials (temperatures and partial pressures). More generally, quantitative prediction of PCT behavior [26–28] is difficult due to the computational cost of density functional theory (DFT) and the required high-throughput sampling of the potential energy surface of hydrogen and metal alloy interactions; nonetheless, tractability has been demonstrated for simpler metal hydride systems at near ambient pressures by combining machine learning surrogate models for DFT and first-principles thermodynamics [29]. However, PCT prediction becomes even more difficult if a metal or alloy is open to multiple species that can populate its interstitials (i.e., H *and* N) or if the pressure range to be modeled is sufficiently high that the pressure contribution to the enthalpy is non-negligible.

Our goal is therefore to generally address both challenges in a unified computational workflow so that PCT behavior of high-pressure, multi-element interstitial hydrides can be more rapidly predicted. We will demonstrate this for the cubic $Lu(H, N, Va)_3$ system, but expect its applicability to translate to other materials science domains relying on (high-pressure) interstitial incorporation in intermetallic alloy lattices. Modern ma-

* pguan@sandia.gov
† mwitman@sandia.gov

chine learning techniques offer the ability to accurately approximate high dimensional functions [30], opening up new possibilities for solving "curse of dimensionality", a key challenge in materials science. We propose the use of graph neural networks (GNNs) [31–33] as surrogate models to directly predict computationally expensive DFT-relaxed properties from an unrelaxed crystallographic representation [29, 34, 35], specifically the zero-pressure *relaxed* formation energy, $E_{f,0}$, and specific volume, ν_0, using just the idealized (i.e., *un-relaxed*) FCC crystallographic lattice and coordinates as inputs. With a sufficiently accurate model for $E_{f,0}$ and ν_0 trained on a reasonable number (∼1,000) of DFT relaxations, the surrogate model used for the extensive sampling required by lattice model Monte Carlo to estimate free energies dependent on composition, pressure and temperature, from which different types of phase equilibria and thermodynamic properties can be calculated. Additionally, we propose a new doping strategy to optimize hydrogen-storage alloys based on thermodynamic modeling. By facilitating the assessment of thermodynamic stability of high H-content hydrides, we anticipate this general approach will help with future rational design strategies to reduce the extreme pressures needed for their synthesis, as well as provide an efficient approach for thermodynamic modeling of multi-component solid solutions as an alternative to the conventional method based on cluster expansion (CE). Finally, we conclude with some insights into current limitations and the promising opportunities for extending this work in the future.

RESULTS AND DISCUSSION

Our workflow for computing pressure-dependent thermodynamics in compositionally complex solid solutions is graphically summarized in Figure 1 and discussed in detail below. The major steps consist of the following: (a,b) high-throughput sampling and first principles calculations of solid solution configurations are used to fit equation-of-state parameters, (c) GNN training to predict these configuration-dependent parameters using the idealized starting structure as input, (d) Monte Carlo simulations of pressure-dependent enthalpies, (e) calculation of Gibbs energies and phase diagrams.

High-throughput sampling of Lu-N-H system

First we generate 1,179 2x2x2 ideal FCC supercell configurations, $\mathbf{X_{FCC}}$, of $\mathrm{Lu(H,N)}_{3-x}$. Each initial configuration, consisting only of Lu at each packing site, differs only by the identity (N, H, or Va) of the octahedral and tetrahedral interstitials. For each initial configuration, we relax the structure at zero-pressure and zero-temperature to obtain $E_{f,0}$ and ν_0, after which energy vs. volume calculations are used to fit the Rose-Vinet equation of state [36] and obtain the bulk modulus and pressure derivative of the bulk modulus, B and B', respectively. Each calculation, especially the fitting of B and B', and time-intensive and there are nominally $3^{12} \approx$ 500k possible assignments of (H,N,Va) to the interstitial sites in the 1x1x1 FCC unit cell alone, let alone the $3^{(12\cdot 8)}$ possible assignments in the 2x2x2 supercell. An efficient surrogate model for the equation of state parameters of a given configuration, coupled to Monte Carlo simulations, are therefore clearly needed to effectively sample phase space for phase diagram construction. The brute-force DFT-sampled potential energy landscape from the ∼1200 configuration training data is shown in Figure 2(a) as a function of $\mathrm{x_H}$ and $\mathrm{x_{Lu}}$. To construct Figure 2(b), we compute the standard deviation, σ, of a configuration's nearest neighbor Lu-Lu interatomic distances, then summarize the data as a box-and-whisker plot, grouping configurations by $\mathrm{x_N}$. This indicates that, as expected, higher N concentrations are more likely than higher H concentrations to introduce larger structural distortions to the idealized FCC lattice where $\sigma = 0$.

GNN surrogate model validation

Figure 3's top and bottom rows summarize the performance of our trained GNN models on the $E_{f,0}$ and v_0 prediction tasks, respectively. For each prediction target, three versions of parity plot for the combined $K = 10$-fold test set predictions are differentiated by color-coding either H content ($\mathrm{x_H/x_{Lu}}$), N content ($\mathrm{x_N/x_{Lu}}$), or the data density. The parity plots immediately reveal that low $E_{f,0}$ is correlated with high N content. Additionally, we plot the expectation mean absolute error (MAE) and R^2 across K-fold test sets, $\langle \mathrm{MAE} \rangle_K$ and $\langle R^2 \rangle_K$, respectively, as a function of $\mathrm{x_N/x_{Lu}}$ where any configurations with a higher N content are excluded from performance metric. This reveals critical insight into model performance: for $\mathrm{x_N}/x_{\mathrm{Lu}} < 0.5$ we can achieve expected MAE of < 40 meV/atom and $R^2 > 0.9$ but performance starts to deteriorate for $\mathrm{x_N}/x_{\mathrm{Lu}} > 0.5$. This generally arises because high N content configurations undergo significant distortion from the ideal FCC lattice and interstitial geometry (Figure 2b), meaning the actual structure deviates further from the idealized lattice that must be used as input to the ML model. Note that increasing MAE with increasing $\mathrm{x_N/x_{Lu}}$ is due to a relative error increase as well since R^2 also begins to drop for higher N content configurations. This insight bounds the expected accuracy of the subsequent phase diagram predictions as a function of N content. Finally, we were unable to train a sufficiently accurate model for B or B' to be useful in any predictive capacity. However, we hypothesize this could be possible in the future with additional training data and/or more advanced (equivariant) model architectures since, for example, full elasticity tensors be predicted, albeit within a more diverse chemical and structural space [37].

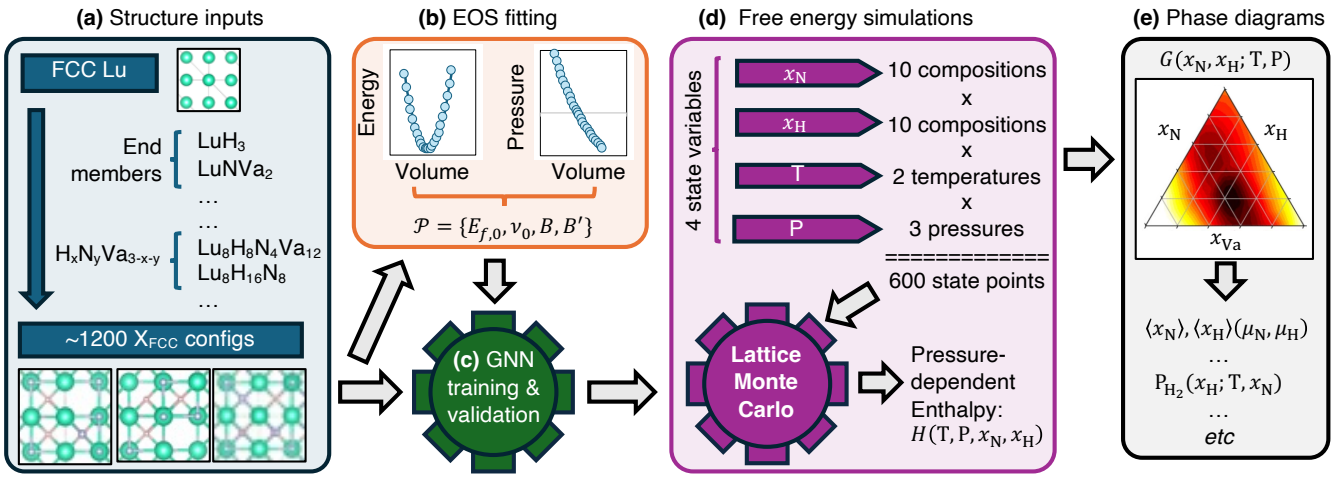

FIG. 1. Graphical summary of the machine learning-accelerated workflow for calculating pressure-dependent thermodynamics of compositionally complex solid solutions. (a) Solid solution configurations on an idealized lattice, $\mathbf{X_{FCC}}$, are first generated by sampling different end member and intermediary compositions. (b) Configuration-dependent energy and pressure vs. volume curves are fit to an equation of state to extract a set of 4 parameters, $\mathcal{P}$: zero-pressure formation energy ($E_{f,0}$), zero-pressure volume (ν_0), bulk modulus (B), and pressure-derivative of bulk modulus (B'). (c) GNN surrogate models are trained to predict these properties using $\mathbf{X}_{\mathrm{FCC}}$ as input. (d) A multitude of lattice Monte Carlo simulations across fixed composition, temperature, and pressure are performed using the GNN models. (e) Gibbs free energies as a function of composition, temperature, and pressure are computed, from which relevant macroscopic properties can be computed (which may be complicated to experimentally extract), such as expected composition as a function of chemical potentials, $\langle \mathrm{x_N} \rangle, \langle x_{\mathrm{H}} \rangle (\mu_{\mathrm{N}}, \mu_{\mathrm{H}})$, or the temperature-dependent equilibrium hydrogen pressure as a function of concentrations, $\mathrm{P}_{\mathrm{H_2}}(x_{\mathrm{H}}; \mathrm{T}, x_{\mathrm{N}})$.

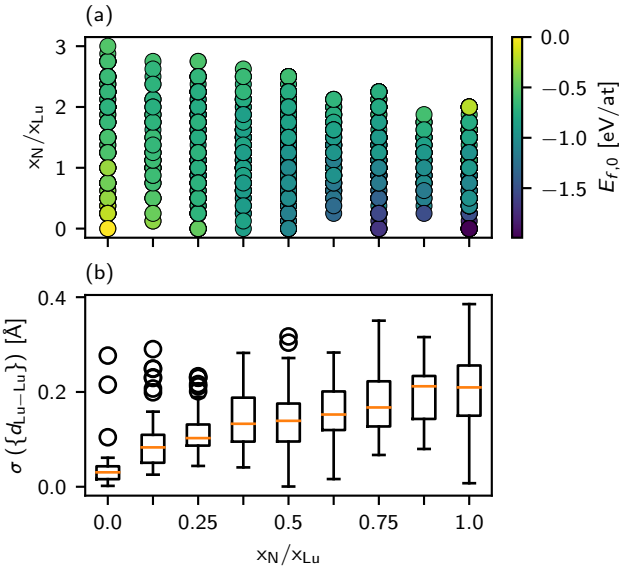

FIG. 2. (a) The DFT calculated formation energies of training configurations as a function of $\mathrm{x_H/x_{Lu}}$ and $\mathrm{x_N/x_{Lu}}$. (b) For each configuration, the standard deviation of all nearest neighbor Lu-Lu interatomic distances, $\sigma(\{d_{\mathrm{Lu-Lu}}\})$, is computed and summarized as a box-and-whisker by grouping configurations for a given $\mathrm{x_N/x_{Lu}}$.

Gibbs energies and phase equilibria of cubic $\mathbf{Lu(H, N, Va)_3}$

The Monte Carlo (MC) simulations were employed to calculate Gibbs energies at a fixed chemical composition, temperature and pressure. The enthalpy is obtained by

$$\mathrm{H} = \sum_{\alpha} (\mathrm{E}_{\alpha} + \mathrm{PV}_{\alpha})\, \rho_{\alpha} \tag{1}$$

where E_{α} and V_{α} is energy and volume of a sampled configuration α respectively, P is pressure, and ρ_{α} is the frequency of the configuration α appearing in the simulation. We have the exact differential

$$\mathrm{d}(\beta \mathrm{G}) = \mathrm{d}(\beta(\mathrm{H} - \mathrm{TS})) = \mathrm{H}\mathrm{d}\beta + \beta \mathrm{V}\mathrm{d}\mathrm{P} \tag{2}$$

where G is the Gibbs energy, $\beta = 1/\mathrm{k_B T}$, $\mathrm{k_B}$ is Boltzmann constant, and T is temperature. Using $\lim_{\beta \to 0} \beta \mathrm{G} = \Sigma \mathrm{c_i} \ln \mathrm{c_i}$, where c_i is the site fraction of species i (i=H, N, Va) in the interstitial sites, the Gibbs energy at temperature T, pressure P and compositions $\mathrm{x_H}$ and $\mathrm{x_N}$ can be calculated as

$$\beta \mathrm{G}(\mathrm{T}, \mathrm{P}, \mathrm{x_H}, \mathrm{x_N}) = \Sigma \mathrm{c_i} \ln \mathrm{c_i} + \int_0^{\beta} \mathrm{H}(\beta', \mathrm{P}, \mathrm{x_H}, \mathrm{x_N}) \mathrm{d}\beta'. \tag{3}$$

Gibbs energies of the cubic $\mathrm{Lu(H, N, Va)_3}$ solid solution under three pressures (0, 1, 2 GPa) and two temperatures (273, 1273 K) are shown in Figure 4. More details including site occupancies of each species, the MC-sampled distribution of enthalpies of configurations and

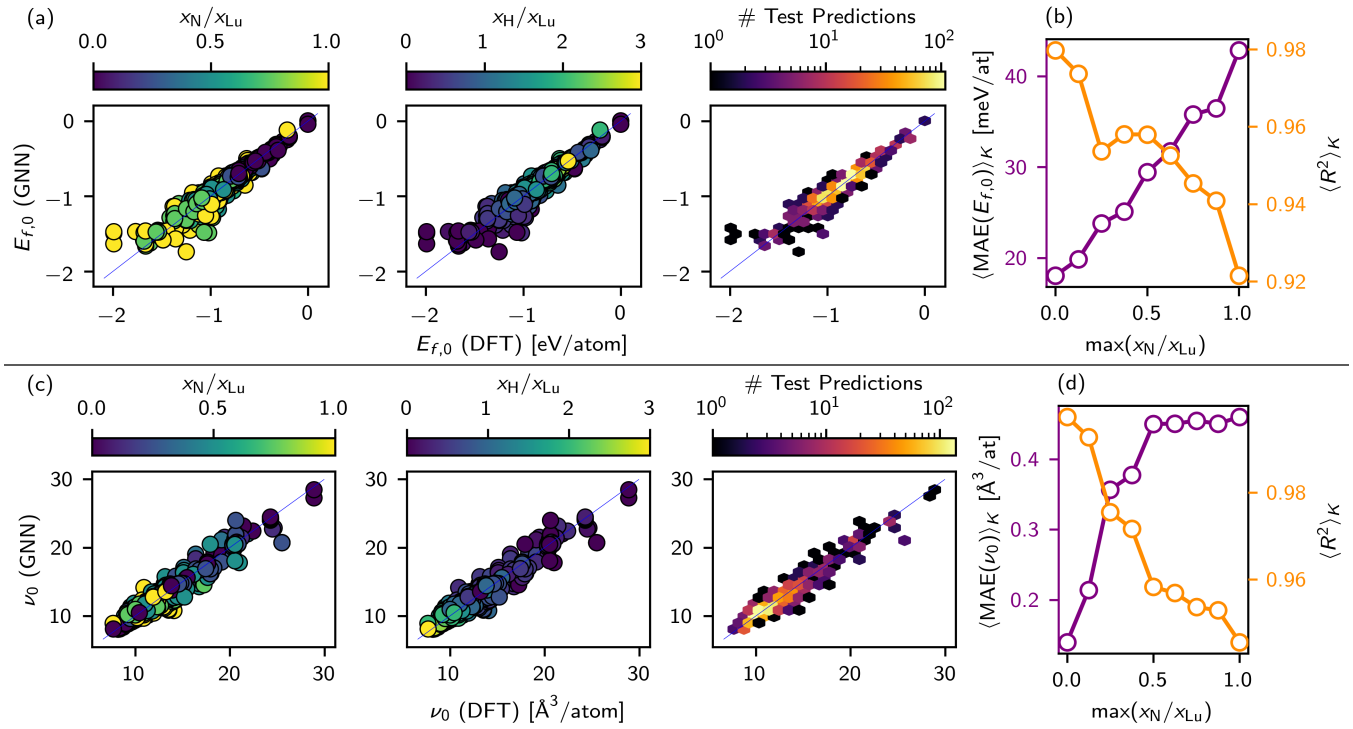

FIG. 3. Model validation for (a,b)$E_{f,0}$ and (c,d) ν_0 predictions. Parity plots (a,c) correspond to the combined $K = 10$-fold test set predictions, differentiated by color-coding H content (x_H/x_{Lu}), N content (x_N/x_{Lu}), or the data density. (b,d) show expected (K-fold averaged test set) MAE R^2 in purple and orange, respectively, as a function of the maximum x_N/x_{Lu} considered.

plots of Gibbs energies as functions of temperature can be found in the Supplementary Information. The Gibbs energies are most sensitive with respect to x_N, most negative when $x_N/x_{Lu} \sim 1$, and increase drastically when x_N further increases. Notably, the Gibbs energy surfaces are non-convex, with multiple local minima, indicating immiscibility between the three constituents H, N and vacancy within the interstitial sites. The temperature and pressure up to 2 GPa have an effect on, but do not majorly alter, the features of the Gibbs energy surfaces fundamentally.

Based on the calculated Gibbs energies, the ternary phase equilibria of cubic $Lu(H, N, Va)_3$ are computed and shown in Figure 5 for different combinations of temperatures and pressures. Instead of compositions, chemical potentials (μ_H and μ_N) are chosen as the diagram axes since they are control variables for H and N more frequently in experiments and can be tuned via temperature and partial pressure when these components are in a vapor state. However, it should be noted that here the phase equilibria are calculated for the cubic Lu-H-N phases only without assuming a solid-vapor equilibrium, otherwise the total four conditions (T, P, μ_H, and μ_N) cannot be varied independently according to the phase rule. Within the range of conditions shown in the figures, there are four phase regions, i.e., $LuH_{3-x}N_y$, $LuH_{2\pm x}N_{1-y}$, $LuH_{0.7\pm x}N_{1\pm y}$ and $LuH_{0.5\pm x}N_{1\pm y}$. The composition changes discontinuously across the phase boundaries, while it changes gradually within each single phase region. Due to the fact that the GNN energy model has increasing errors when $x_N/x_{Lu} > 1$ and the high sensitivity of calculated phase boundaries with respect to Gibbs energy errors, it is possible that the relatively small composition discontinuity between the two H-poor phases $LuH_{0.7\pm x}N_{1\pm y}$ and $LuH_{0.5\pm x}N_{1\pm y}$ may be artifacts and they belong to the same continuous solid solution. With temperature increasing, $LuH_{0.7\pm x}N_{1\pm y}$ has a larger phase region, mainly due to its larger configurational entropy since it has more equal fractions of H, N and vacancy compared with the other phases. A decreasing H stoichiometry with increasing temperature is observed for the $LuH_{3-x}N_y$ phase, due to the entropy effect similarly. With pressure increasing, both H-rich $LuH_{3-x}N_y$ and N-rich $LuH_{0.7\pm x}N_{1\pm y}$ have expanded phase regions, while the $LuH_{2\pm x}N_{1-y}$ phase with significant fractions of both H and N shrinks, indicating the larger immiscibility between H and N under pressure.

An important conclusion from Figure 5 is that it is difficult to achieve significant N-doping levels in the $LuH_{3-x}N_y$ phase under thermodynamic equilibrium, which agrees with some experimental works where no or low N content ($x_N/x_{Lu} \leq 0.02$) were detected [25, 38]. Evidently, equilibrium N concentration in $LuH_{3-x}N_y$ is significant only at near-ambient pressures with $\mu_H > 0.7$ eV and $\mu_N > -0.7$ eV and μ_H much larger than μ_N, a region close to the $LuH_{3-x}N_y/LuH_{2\pm x}N_{1-y}$ phase bound-

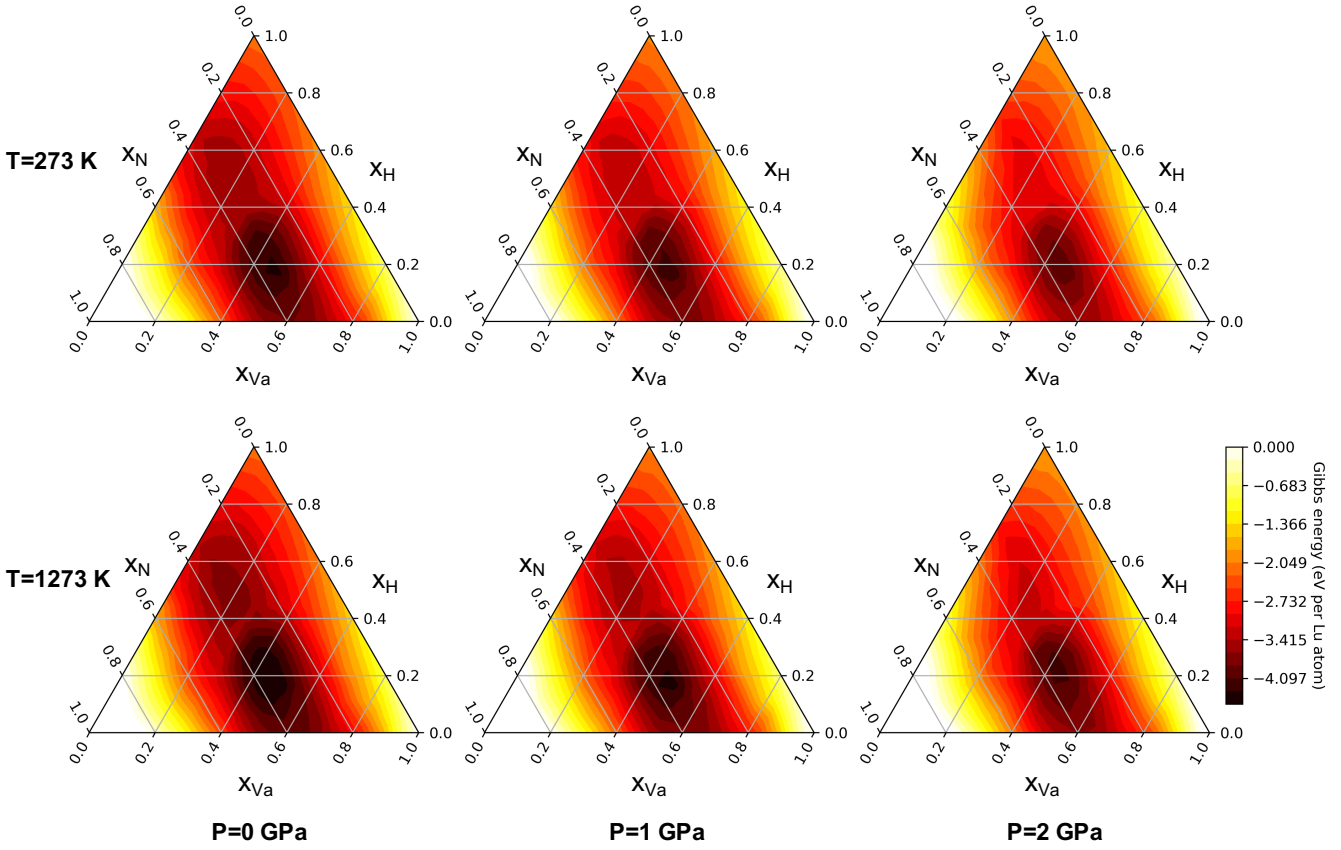

FIG. 4. Gibbs energies of the cubic $Lu(H, N, Va)_3$ solid solution under different pressures and temperatures. The reference states are the elements at their standard states.

ary. However, providing such a high H chemical potential at near-ambient pressures is quite difficult using conventional methods, although non-conventional methods such as the pressure-potential approach introducing electrochemical driving force have been proposed for this purpose [13, 14]. For H_2 in equilibrium with the hydrides, increasing pressure can increase μ_H, but lower equilibrium N solubility in $LuH_{3-x}N_y$ at the same time. Despite this, it is noted that there have been other experimental studies reporting successful synthesis of Lu hydrides with a significant N content under high pressures [18, 19]. In the work by Xing et al. [19], the averaged nitrogen content was 0.84 wt.%, i.e., $x_N/x_{Lu} = 0.11$. If the presence of N is not due to incorporation of secondary phases, then it is very likely that the reported samples are non-equilibrium phases with supersaturated N solutes, based on the present calculations.

Para-equilibrium of cubic $Lu(H, N, Va)_3$ at fixed N-doping levels

When there is a large difference in mobility of different components in a solid solution, instead of a full equilibrium, a temporary para-equilibrium state may occur, where rapidly diffusing elements reach equilibrium while slowly diffusing elements are treated as as immobile [39]. In a para-equilibrium, the ratios of molar fractions of immobile components are the same in all phases. The concept of para-equilibrium has been applied in hydrogenation of alloys, where metal atoms were treated as immobile and H atoms were treated as mobile [40]. Here, based on the fact that the diffusivity of H in metals is much higher than that of heavy interstitials like O and N [41], we calculate para-equilibrium of the cubic $Lu(H, N, Va)_3$ solid solution by assuming: (1) the diffusion of N atoms can be ignored and (2) H atoms are mobile enough to reach equilibrium between different phases. Such para-equilibrium can be obtained from minimization of Gibbs energies at fixed N-doping levels. In addition, we assume the Lu-H-N solids are in equilibrium with a H_2/N_2 fluid phase, thus we can include partial pressures as condition variables. We are most interested in low N compositions, which indicates that μ_H needs to be much larger than μ_N based on Figure 5 and therefore the fluid phase pressure is dominanted by H_2 with $P \approx P_{H_2}$, where P_{H_2} is partial pressure of H_2. The following equation is used to correlate chemical potential and partial pressure of H_2:

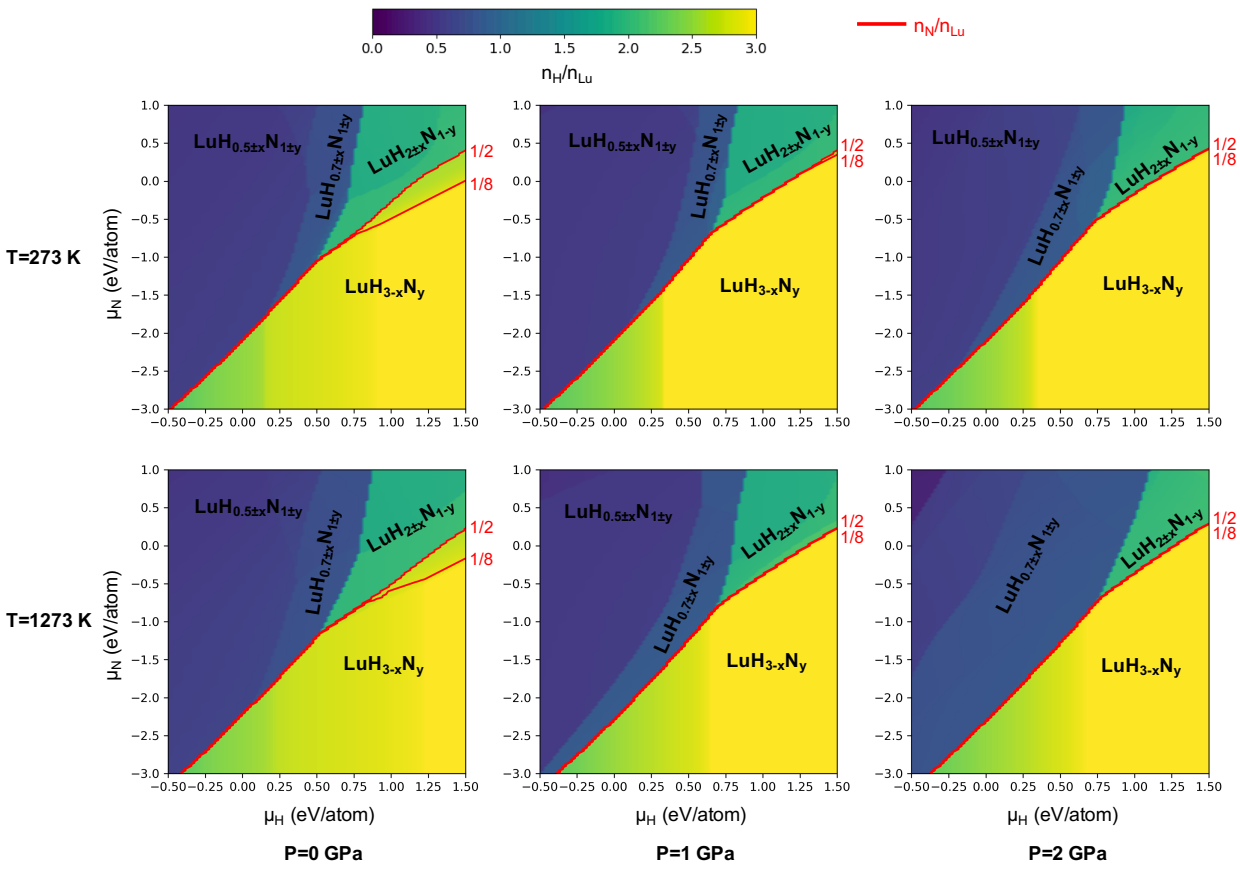

FIG. 5. Equilibrium phase diagrams of the cubic $Lu(H, N, Va)_3$ solid solution under different pressures and temperatures.

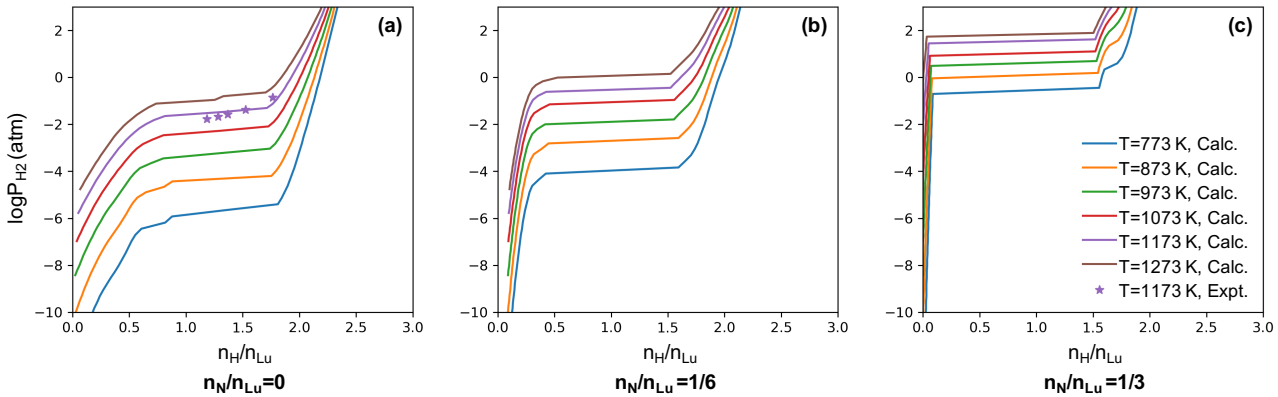

FIG. 6. Para-equilibrium pressure-composition-temperature isotherms of the cubic $Lu(H, N, Va)_3$ solid solution at fixed N-doping levels under near-ambient pressures.

$$\mu_{H_2}(T, P_{H_2}) = \mu_{H_2}(T, P_0) + k_B T \ln\left(\frac{P_{H_2}}{P_0}\right) + k_B T \ln \gamma_{H_2}. \quad (4)$$

We choose 1 bar (0.1 MPa) for the reference hydrogen partial pressure P_0, and k_B is the Boltzmann constant. γ_{H_2} is the fugacity coefficient of H_2, and is calculated using the model of Joubert [42]. $\mu_{H_2}(T, P_0)$ can be written as

$$\mu_{H_2}(T, P_0) = E_{H_2}(P_0) + \Delta\mu_{H_2}(T, P_0), \quad (5)$$

where $E_{H_2}(P_0)$ is the DFT-computed energy of a H_2 molecule at reference pressure, while $\Delta\mu_{H_2}(T, P_0)$ is the finite-temperature contribution. In the present work, $\Delta\mu_{H_2}(T, P_0) = -\Delta S_f^0 T$ with $\Delta S_f^0 = 136$ J/mol/K is used [43]. This term describes the finite-temperature

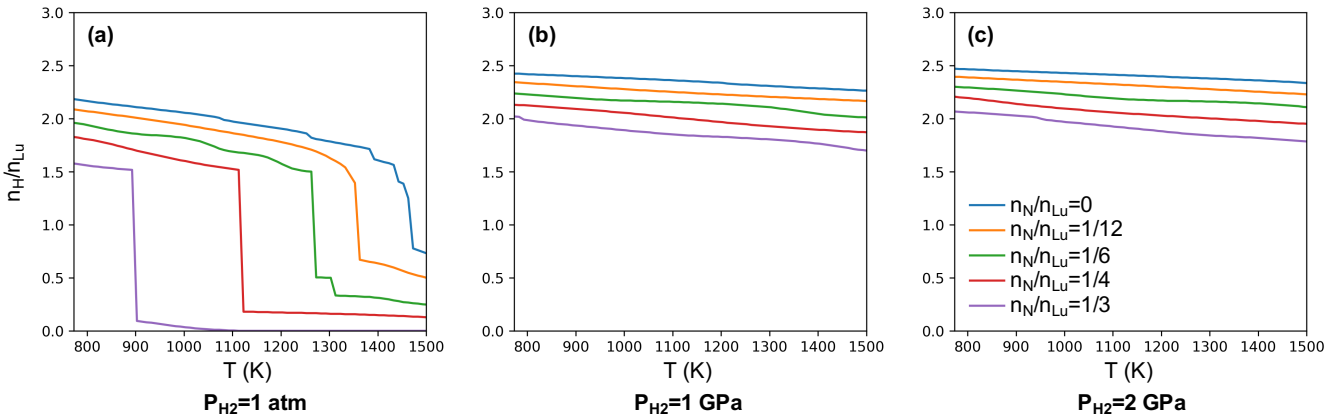

FIG. 7. Temperature-dependent para-equilibrium H composition of the cubic $Lu(H, N, Va)_3$ solid solution at fixed N-doping levels under different pressures.

part of standard Gibbs energy change of LuH_2=Lu+H_2 in 565-950 °C range quite well. By this we implicitly consider the vibrational contributions to Gibbs energies of solids in an approximate way.

The para-equilibrium pressure-composition-temperature (PCT) isotherms of the cubic $Lu(H, N, Va)_3$ solid solution at several fixed N-doping levels under near-ambient pressures are shown in Figure 6. These PCT isotherms all show plateau pressures within certain composition ranges due to equilibrium between an H-poor phase and an H-rich phase, which is a usual feature of metal-hydrogen systems. To our best knowledge, the only available experimental PCT data within the whole Lu-H-N system are those measured for the binary Lu-H system in the temperature range 824-950 °C [43]. The agreement between the present calculations and the experimental data is quite good, demonstrating the validity of our approach. It is evident that, regardless of the N-doping level and within near-ambient pressures (<1000 atm), synthesizing a cubic $Lu(H, N, Va)_3$ phase with $x \gtrsim 2.5$ by pure chemical hydrogenation using fluid H_2 is quite challenging, which necessitates introducing pressures in the GPa level by other driving forces. Remarkably, the N-doping level can significantly change the PCT isotherms. A higher N-doping level leads to orders of magnitude higher plateau pressures, only slightly smaller maximum H capacities, and steeper shapes of the PCT isotherms.

The temperature-dependent para-equilibrium H compositions of the cubic $Lu(H, N, Va)_3$ solid solution at several fixed N-doping levels are shown in Figure 7. The general trend under different pressures is the decrease of H composition with increasing temperature, regardless of the N-doping level. At $P_{H_2} = 1atm$, a phase transition between H-rich and H-poor occurs at a critical temperature T_{dehyd}, which corresponds to the hydrogenation/dehydrogenation temperature. Clearly, T_{dehyd} is very sensitive with respect to the N-doping level. Compared with the undoped Lu-H phase, a N-doping concentration of $x_N/x_{Lu} = 1/3$ can lower T_{dehyd} by more than 600 K, although the maximum H capacity is also lowered at the same time as discussed above. At $P_{H_2} = 1$ GPa and $P_{H_2} = 2$ GPa, no transition to a H-poor phase is observed up to 1473 K within the studied temperature range.

The remarkable effects of the N-doping level on the PCT isotherms and T_{dehyd} imply an anion-doping strategy to optimize thermodynamic behaviors of metal hydrides. A major problem for some of the highest capacity hydrogen-storage alloys, such as Mg-based alloys [44] or refractory metal-based high entropy alloys [45, 46], is their high T_{dehyd}. Doping is well-known to destabilize metal hydrides [47], but previous efforts mainly focused on cation-doping, which may be subjected to some limitations like cost of the dopants and weight increase. If this strategy can be generalized to those materials systems, i.e., a moderate anion-doping can significantly lower T_{dehyd} with a small trade-off in maximum H capacity, superior hydrogen-storage alloys can be made. We note that the complex hydrides also feature incorporation of N or B, but in a much larger amount. One disadvantage of complex hydrides is the great difficulties in reversing the hydrogen release reaction, while the anion-doping strategy may circumvent such drawback. Although one possible hurdle for applying the new strategy may be synthesizing a hydrogen-storage alloy/hydride with supersaturated N solutes without N-rich secondary phases, some experimental studies have reported successful high-pressure synthesis of Lu hydrides with significant N-doping [18, 19]. Experimental explorations are desirable for verifying the anion-doping strategy, which may lead to hydrogen-storage alloys with superior performance.

CONCLUSIONS

In conclusion, we developed an *ab initio* thermodynamic approach by combining Monte Carlo simulation

and GNN models trained on first-principles data. This approach can be used to predict pressure-dependent thermodynamics and phase equilibria of multi-component solid solutions, as exemplified by the cubic Lu-H-N phases. An integral expression is formulated to calculate pressure-dependent Gibbs energies from enthalpies, which can be obtained from MC simulations. The MC simulations use a potential energy model based on a GNN (instead of the conventional CE approach) which achieves chemical accuracy in cross-validated relaxed energy and volume test set predicitions using the idealized fcc lattice structure as input.

Based on the calculated Gibbs energies, phase equilibria of cubic Lu-H-N phases are predicted under different pressures and temperatures. Under full thermodynamic equilibrium, N solubility in $LuH_{3-x}N_y$ is quite small, which leads to a hypothesis that the experimentally reported N-doped Lu hydride samples are likely to be non-equilibrium phases with supersaturated N solutes or contain secondary N-rich phases. Considering the large difference between interstitial H and N mobilities, para-equilibrium of cubic $Lu(H, N, Va)_3$ at fixed N-doping levels are calculated, showing good agreement with experimental data. N-doping levels can significantly modify thermodynamic properties, such as the dehydrogenation temperature, indicating a potential anion-doping strategy to optimize performances of hydrogen-storage alloys.

We expect this work to provide a general approach to model thermodynamics of multi-component solid solutions efficiently, which will be especially useful for compositionally complex materials such as high-entropy alloys, high-entropy ceramics and mixed-anion compounds. It also offers a first-principles method that can be integrated into semi-empirical frameworks of thermodynamic modeling like CALPHAD (CALculation of PHAse Diagrams) [48–50] and its deep learning counterpart [51]. The approach can be further extended to systems with lower dimension like surfaces, with applications in high-entropy catalysts [52, 53]. The approach can be also further accelerated by introducing other machine learning techniques such as active learning [54, 55] for labeling the data needed for training the GNN model.

METHODOLOGY

First-principles calculations

All DFT calculations were done with the Perdew–Burke–Ernzerhof (PBE) [56] exchange correlation functional using the Quantum Espresso software. A plane wave basis expanded up to 42 Ry is used for the representation of electronic wavefunctions, and a k-point density of larger than 20 Å in reciprocal space was used in each dimension. For each structure, the geometry is relaxed to satisfy the convergence criterion that all components of all forces are smaller than 0.001 a.u. and the total energy changes less than 0.0001 Ry. For the solid phases, the Gibbs energies include 0 K total energies and contributions from pressure, while the finite-temperature vibrational contributions are not explicitly calculated. For each pressure, a Vinet equation of state is fitted to find the equilibrium volume that minimizes the Gibbs energy, and the corresponding Gibbs energy is also determined simultaneously.

Monte Carlo simulations

The MC simulations were run at a series of temperatures $5000/i$ K ($i = 1, 2, 3, ...$) and at three pressures 0, 1 and 2 GPa. To sample the composition triangle of $Lu(H, N, Va)_3$, the sampling step along the site fraction of each species (H,N or Va) is 1/18, which leads to 190 sampled compositions in total. For simplicity, the volume fluctuation around the equilibrium value for each configuration is neglected. The average energy in each MC simulation is converged to 0.001 eV. The enthalpy of the solid solution phase can then be calculated from the ensemble average using Equation 1, which can be used to calculate Gibbs energy based on Equation 3.

Graph neural network models

We train a GNN, parameterized by model weights, θ, to predict DFT-computed Vinet equation of state parameters, P, for a given solid solution configuration from its ideal (unrelaxed) FCC crystal structure representation, $\mathbf{X}_{\mathrm{FCC}}$,

$$\{\mathcal{P}\} = f_{\mathrm{GNN}}(\mathbf{X}_{\mathrm{FCC}}; \theta). \tag{6}$$

Any input structure therefore has identical lattice vectors and metal/interstitial site coordinates, while the only difference between them is the population or absence of N or H at the possible octahedral or tetrahedral interstitial sites. Here, the fitted parameters we wish to predict are $\mathcal{P} = \{E_0, V_0, B, B'\}$, which correspond to the energy at zero pressure, the volume at zero pressure, the equilibrium bulk modulus, and its pressure derivative. To aid in model training we convert E_0 to the formation energy at zero pressure, $E_{f,0}$ and convert V_0 to the volume per atom at zero pressure ν_0.

While a plethora of increasingly complex and accurate GNN methodolgies [31–33] have been proposed for materials science applications in recent years, we utilize here the cystal graph convolutional neural network (CGCNN) formalism [31] since it facilitates training in low data regimes ($\sim 10^3$ or less training examples) by maintaining sufficiently expressive models with low parameter complexity. The method is re-summarized here with the minor modifications made for the GNNs trained in this work.

1. The idealized crystal structure $\mathbf{X_{FCC}}$ is constructed as a graph with nodes corresponding to

atoms and edges representing connections between neighboring atoms with distance less than a cutoff radius, $r_c = 4.5$ Å.

2. The initial node feature vector of atomic site i, $\boldsymbol{v}_i^{(t=0)}$, is generated by one-hot encoding its atomic number. Initial edge features between neighbors i and j, $\boldsymbol{b}_{ij}$, are encoded by two-body symmetry functions [57] of the bond distance according to a set of Gaussian widths (η), centers (R_s), r_c, and a cutoff function, f_c:

$$\boldsymbol{b}_{ij} = \{\exp\left[-\eta(r_{ij} - R_s)^2\right] f_c(r_{ij})\}. \tag{7}$$

Here we use $\eta = \{0.5, 1.0, 1.5\}$, $R_s = \{1.0, 2.0, 3.0, 4.0, 5.0\}$, and

$$f_c(r_{ij}) = \begin{cases} \left(\cos\left(\frac{\pi r_{ij}}{r_c}\right) + 1\right)/2 & \text{for } r_{ij} \leq r_c \\ 0 & \text{for } r_{ij} > r_c \end{cases} \tag{8}$$

3. At each convolution layer, t, node feature vectors are updated according to the following filter:

$$\boldsymbol{v}_i^{(t+1)} = g\left(\boldsymbol{v}_i^{(t)} + \sum_j \sigma\left(\boldsymbol{z}_{ij}^{(t)}\boldsymbol{W}_1^{(t)} + \boldsymbol{b}_1^{(t)}\right) \odot g\left(\boldsymbol{z}_{ij}^{(t)}\boldsymbol{W}_2^{(t)} + \boldsymbol{b}_2^{(t)}\right)\right). \tag{9}$$

Here $\boldsymbol{z}_{ij} = \boldsymbol{v}_i \oplus \boldsymbol{v}_j \oplus \boldsymbol{b}_{ij}$ is the concatenation of features between connected nodes in the graph, $\boldsymbol{W}_1$,$\boldsymbol{W}_2$ and b_1, b_2 represent weights and biases of different learnable weight matrices (i.e., fully connected neural network layers), σ denotes a sigmoid activation function, g denotes a softplus activation, and $\odot$ denotes element-wise multiplication.

4. Following T convolution layers, node feature vectors for all N atoms in the crystal are pooled to compute a global crystal feature vector, $\boldsymbol{v}_c = \text{Pool}\left(\boldsymbol{v}_0^{(T)}, \boldsymbol{v}_1^{(T)}, \ldots, \boldsymbol{v}_N^{(T)}\right)$.

5. Finally, n_h fully connected hidden layers are utilized to predict the relaxed formation energy of the crystal structure, E_f.

All GNN models were constructed and trained with the architecture and hyperparameters in Table I.

Hyperparameter	Value
Node feature vector dimensionality	$\boldsymbol{v}_i^{(t)} \in \mathbb{R}^8$
Number of convolution steps	$T = 3$
Crystal feature vector dimensionality	$\boldsymbol{v}_c \in \mathbb{R}^8$
Number of feed forward layers post-convolutions	$n_h = 2$
Training epochs	1000
Learning rate	0.05
Optimizer	Adam

TABLE I. Architecture and training hyperparameters used for all models in this study.

DATA & CODE AVAILABILITY

FCC Lu-N-H DFT training data is included in the Supplementary Information, which provides cif files of the idealized FCC geometry and equation of state parameters for each configuration (the zero-pressure formation energy, the zero-pressure volume per atom, the bulk modulus, and the pressure derivative of the bulk modulus). The CGCNN code was used to train the lattice GNN models in this study (`https://github.com/txie-93/cgcnn`). The ASE code was used to create a calculator object for the trained GNN models, which are called by the Monte Carlo simulations performed using the ASAP code (`https://gitlab.com/asap/asap`).

ACKNOWLEDGMENTS

The authors gratefully acknowledge research support from the Laboratory Directed Research and Development (LDRD) program at Sandia National Laboratories. Sandia National Laboratories is a multimission laboratory managed and operated by National Technology & Engineering Solutions of Sandia, LLC, a wholly owned subsidiary of Honeywell International Inc., for the U.S. Department of Energy's National Nuclear Security Administration (DOE/NNSA) under Contract DE-NA0003525. This written work is authored by an employee of NTESS. The employee, not NTESS, owns the right, title, and interest in and to the written work and is responsible for its contents. Any subjective views or opinions that might be expressed in the written work do not necessarily represent the views of the U.S. Government. The publisher acknowledges that the U.S. Government retains a non-exclusive, paid-up, irrevocable, worldwide license to publish or reproduce the published form of this written work or allow others to do so, for U.S. Government purposes. The DOE will provide public access to results of federally sponsored research in accordance with the DOE Public Access Plan.

[1] H. Liu, I. I. Naumov, R. Hoffmann, N. W. Ashcroft, and R. J. Hemley, Potential high-Tc superconducting lanthanum and yttrium hydrides at high pressure, Proc. Natl. Acad. Sci. U.S.A. **114**, 6990 (2017).

[2] F. Peng, Y. Sun, C. J. Pickard, R. J. Needs, Q. Wu, and Y. Ma, Hydrogen clathrate structures in rare earth hydrides at high pressures: possible route to room-temperature superconductivity, Phys. Rev. Lett. **119**, 107001 (2017).

[3] Z. M. Geballe, H. Liu, A. K. Mishra, M. Ahart, M. Somayazulu, Y. Meng, M. Baldini, and R. J. Hemley, Synthesis and stability of lanthanum superhydrides, Angew. Chem. Int. Ed. **57**, 688 (2018).

[4] M. Somayazulu, M. Ahart, A. K. Mishra, Z. M. Geballe, M. Baldini, Y. Meng, V. V. Struzhkin, and R. J. Hemley, Evidence for superconductivity above 260 k in lanthanum superhydride at megabar pressures, Phys. Rev. Lett. **122**, 027001 (2019).

[5] A. P. Drozdov, P. P. Kong, V. S. Minkov, S. P. Besedin, M. A. Kuzovnikov, S. Mozaffari, L. Balicas, F. F. Balakirev, D. E. Graf, V. B. Prakapenka, E. Greenberg, D. A. Knyazev, M. Tkacz, and M. I. Eremets, Superconductivity at 250 K in lanthanum hydride under high pressures, Nature **569**, 528 (2019).

[6] Y. Sun, J. Lv, Y. Xie, H. Liu, and Y. Ma, Route to a superconducting phase above room temperature in electron-doped hydride compounds under high pressure, Phys. Rev. Lett. **123**, 097001 (2019).

[7] J. Lv, Y. Sun, H. Liu, and Y. Ma, Theory-orientated discovery of high-temperature superconductors in superhydrides stabilized under high pressure, Matter Radiat. Extremes **5**, 068101 (2020).

[8] K. P. Hilleke and E. Zurek, Rational design of superconducting metal hydrides via chemical pressure tuning, Angewandte Chemie International Edition **61**, e202207589 (2022).

[9] S. Di Cataldo, C. Heil, W. von der Linden, and L. Boeri, La bh 8: Towards high-t c low-pressure superconductivity in ternary superhydrides, Physical Review B **104**, L020511 (2021).

[10] X. Liang, A. Bergara, X. Wei, X. Song, L. Wang, R. Sun, H. Liu, R. J. Hemley, L. Wang, G. Gao, *et al.*, Prediction of high-t c superconductivity in ternary lanthanum borohydrides, Physical Review B **104**, 134501 (2021).

[11] R. Lucrezi, S. Di Cataldo, W. von der Linden, L. Boeri, and C. Heil, In-silico synthesis of lowest-pressure high-t c ternary superhydrides, npj Computational Materials **8**, 119 (2022).

[12] S. Di Cataldo and L. Boeri, Metal borohydrides as ambient-pressure high-t c superconductors, Physical Review B **107**, L060501 (2023).

[13] P.-W. Guan, R. J. Hemley, and V. Viswanathan, Combining pressure and electrochemistry to synthesize superhydrides, Proc. Natl. Acad. Sci. U.S.A. **118**, e2110470118 (2021).

[14] P.-W. Guan, Y. Sun, R. J. Hemley, H. Liu, Y. Ma, and V. Viswanathan, Low-pressure electrochemical synthesis of complex high-pressure superconducting superhydrides, Physical Review Letters **128**, 186001 (2022).

[15] N. Dasenbrock-Gammon, E. Snider, R. McBride, H. Pasan, D. Durkee, N. Khalvashi-Sutter, S. Munasinghe, S. E. Dissanayake, K. V. Lawler, A. Salamat, *et al.*, Retracted article: Evidence of near-ambient superconductivity in a n-doped lutetium hydride, Nature **615**, 244 (2023).

[16] Z. Huo, D. Duan, T. Ma, Z. Zhang, Q. Jiang, D. An, H. Song, F. Tian, and T. Cui, First-principles study on the conventional superconductivity of n-doped fcc-luh3, Matter and Radiation at Extremes **8** (2023).

[17] Y. Sun, F. Zhang, S. Wu, V. Antropov, and K.-M. Ho, Effect of nitrogen doping and pressure on the stability of lu h 3, Physical Review B **108**, L020101 (2023).

[18] X. Ming, Y.-J. Zhang, X. Zhu, Q. Li, C. He, Y. Liu, T. Huang, G. Liu, B. Zheng, H. Yang, *et al.*, Absence of near-ambient superconductivity in luh2±x n y, Nature **620**, 72 (2023).

[19] X. Xing, C. Wang, L. Yu, J. Xu, C. Zhang, M. Zhang, S. Huang, X. Zhang, Y. Liu, B. Yang, *et al.*, Observation of non-superconducting phase changes in nitrogen doped lutetium hydrides, Nature Communications **14**, 5991 (2023).

[20] K. P. Hilleke, X. Wang, D. Luo, N. Geng, B. Wang, F. Belli, and E. Zurek, Structure, stability, and superconductivity of n-doped lutetium hydrides at kbar pressures, Physical Review B **108**, 014511 (2023).

[21] P. P. Ferreira, L. J. Conway, A. Cucciari, S. Di Cataldo, F. Giannessi, E. Kogler, L. T. Eleno, C. J. Pickard, C. Heil, and L. Boeri, Search for ambient superconductivity in the lu-nh system, Nature Communications **14**, 5367 (2023).

[22] F. Xie, T. Lu, Z. Yu, Y. Wang, Z. Wang, S. Meng, and M. Liu, Lu–h–n phase diagram from first-principles calculations, Chinese Physics Letters **40**, 057401 (2023).

[23] R. Lucrezi, P. P. Ferreira, M. Aichhorn, and C. Heil, Temperature and quantum anharmonic lattice effects on stability and superconductivity in lutetium trihydride, Nature Communications **15**, 441 (2024).

[24] A. Denchfield, H. Park, and R. J. Hemley, Electronic structure of nitrogen-doped lutetium hydrides, Physical Review Materials **8**, L021801 (2024).

[25] Y. Han, Y. Ou, H. Sun, J. Kopaczek, G. J. Leonel, X. Guo, B. L. Brugman, K. Leinenweber, H. Xu, M. Wang, *et al.*, Thermodynamic properties and enhancement of diamagnetism in nitrogen doped lutetium hydride synthesized at high pressure, Proceedings of the National Academy of Sciences **121**, e2321540121 (2024).

[26] R. G. Mullen and N. Goldman, Quantum Accurate Prediction of Plutonium–Plutonium Dihydride Phase Equilibrium Using a Lattice Gas Model, J. Phys. Chem. C **124**, 20881 (2020).

[27] Thermodynamic modelling of hydrogen-multicomponent alloy systems: Calculating pressure-composition-temperature diagrams, Acta Mater. **215**, 117070 (2021).

[28] Design of multicomponent alloys with C14 laves phase structure for hydrogen storage assisted by computational thermodynamic, Acta Mater. **240**, 118317 (2022).

[29] M. D. Witman, N. C. Bartelt, S. Ling, P.-W. Guan, L. Way, M. D. Allendorf, and V. Stavila, Phase Diagrams of Alloys and Their Hydrides via On-Lattice Graph Neural Networks and Limited Training Data, J. Phys. Chem. Lett. **15**, 1500 (2024).

[30] E. Weinan, Machine learning and computational mathematics, arXiv preprint arXiv:2009.14596 (2020).

[31] T. Xie and J. C. Grossman, Crystal Graph Convolutional Neural Networks for an Accurate and Interpretable Prediction of Material Properties, Phys. Rev. Lett. **120**, 145301 (2018), arXiv:1710.10324.

[32] K. Choudhary and B. DeCost, Atomistic Line Graph Neural Network for improved materials property predictions, npj Comput. Mater. **7**, 185 (2021).

[33] O. T. Unke, S. Chmiela, M. Gastegger, K. T. Schütt, H. E. Sauceda, and K.-R. Müller, SpookyNet: Learning force fields with electronic degrees of freedom and nonlocal effects, Nat. Commun. **12**, 7273 (2021), arXiv:2105.00304.

[34] J. Gibson, A. Hire, and R. G. Hennig, Data-augmentation for graph neural network learning of the relaxed energies of unrelaxed structures, npj Comput. Mater. **8**, 211 (2022).

[35] M. D. Witman, A. Goyal, T. Ogitsu, A. H. McDaniel, and S. Lany, Defect graph neural networks for materials discovery in high-temperature clean-energy applications, Nat. Comput. Sci. **3**, 675 (2023).

[36] P. Vinet, J. Ferrante, J. H. Rose, and J. R. Smith, Compressibility of solids, J. Geophys. Res. Solid Earth **92**, 9319 (1987).

[37] M. Wen, M. K. Horton, J. M. Munro, P. Huck, and K. A. Persson, An equivariant graph neural network for the elasticity tensors of all seven crystal systems, Digit. Discov. **3**, 869 (2024), arXiv:2307.15242.

[38] S. Cai, J. Guo, H. Shu, L. Yang, P. Wang, Y. Zhou, J. Zhao, J. Han, Q. Wu, W. Yang, *et al.*, No evidence of superconductivity in a compressed sample prepared from lutetium foil and h2/n2 gas mixture, Matter and Radiation at Extremes **8** (2023).

[39] M. Hillert, *Phase equilibria, phase diagrams and phase transformations: their thermodynamic basis* (Cambridge university press, 2007).

[40] E. Alvares, P. Jerabek, Y. Shang, A. Santhosh, C. Pistidda, T. W. Heo, B. Sundman, and M. Dornheim, Modeling the thermodynamics of the feti hydrogenation under para-equilibrium: An ab-initio and experimental study, Calphad **77**, 102426 (2022).

[41] J. Völkl and G. Alefeld, Diffusion of hydrogen in metals, Hydrogen in Metals I: Basic Properties , 321 (2005).

[42] J.-M. Joubert, A calphad-type equation of state for hydrogen gas and its application to the assessment of rh–h system, International journal of hydrogen energy **35**, 2104 (2010).

[43] P. Subramanian and J. Smith, Hydrogen vapor pressure measurements over a portion of the lu-h system, Journal of the Less Common Metals **87**, 205 (1982).

[44] Magnesium- and intermetallic alloys-based hydrides for energy storage: modelling, synthesis and properties, Prog. Energy **4**, 032007 (2022).

[45] M. Sahlberg, D. Karlsson, C. Zlotea, and U. Jansson, Superior hydrogen storage in high entropy alloys, Sci. Rep. **6**, 36770 (2016).

[46] Towards Pareto optimal high entropy hydrides via data-driven materials discovery, J. Mater. Chem. A **11**, 15878 (2023).

[47] M. D. Allendorf, V. Stavila, J. L. Snider, M. Witman, M. E. Bowden, K. Brooks, B. L. Tran, and T. Autrey, Challenges to developing materials for the transport and storage of hydrogen, Nature Chemistry **14**, 1214 (2022).

[48] H. Lukas, S. G. Fries, and B. Sundman, *Computational thermodynamics: the Calphad method* (Cambridge university press, 2007).

[49] Z.-K. Liu, First-principles calculations and calphad modeling of thermodynamics, Journal of phase equilibria and diffusion **30**, 517 (2009).

[50] M. Palumbo, E. Dematteis, L. Fenocchio, G. Cacciamani, and M. Baricco, Advances in calphad methodology for modeling hydrides: A comprehensive review, Journal of Phase Equilibria and Diffusion , 1 (2024).

[51] P.-W. Guan, Differentiable thermodynamic modeling, Scripta Materialia **207**, 114217 (2022).

[52] T. A. Batchelor, J. K. Pedersen, S. H. Winther, I. E. Castelli, K. W. Jacobsen, and J. Rossmeisl, High-entropy alloys as a discovery platform for electrocatalysis, Joule **3**, 834 (2019).

[53] Y. Sun and S. Dai, High-entropy materials for catalysis: A new frontier, Science Advances **7**, eabg1600 (2021).

[54] T. Lookman, P. V. Balachandran, D. Xue, and R. Yuan, Active learning in materials science with emphasis on adaptive sampling using uncertainties for targeted design, npj Computational Materials **5**, 21 (2019).

[55] K. Gubaev, E. V. Podryabinkin, G. L. Hart, and A. V. Shapeev, Accelerating high-throughput searches for new alloys with active learning of interatomic potentials, Computational Materials Science **156**, 148 (2019).

[56] J. P. Perdew, K. Burke, and M. Ernzerhof, Generalized gradient approximation made simple, Phys. Rev. Lett. **77**, 3865 (1996).

[57] J. Behler and M. Parrinello, Generalized neural-network representation of high-dimensional potential-energy surfaces, Phys. Rev. Lett. **98**, 1 (2007).